Stability Analysis of Ice Crystal Orientation

XIPING ZENG,[a] ZBIGNIEW ULANOWSKI,[b,c] ANDREW J. HEYMSFIELD,[d] YANSEN WANG,[a] AND XIAOWEN LI[e,f]

[a] *Army Research Laboratory, Adelphi, Maryland*
[b] *British Antarctic Survey, Cambridge, United Kingdom*
[c] *University of Manchester, Manchester, United Kingdom*
[d] *National Center for Atmospheric Research, Boulder, Colorado*
[e] *NASA Goddard Space Flight Center, Greenbelt, Maryland*
[f] *Morgan State University, Baltimore, Maryland*

(Manuscript received 14 October 2022, in final form 30 March 2023, accepted 1 April 2023)

ABSTRACT: The stability of ice crystal orientation is studied by modeling the airflow around ice crystals at moderate Reynolds number, where an ice crystal is approximated by a cylinder with three parameters: diameter D, length L, and zenith angle of the axis θ. In this paper, the torque acting on ice crystals is simulated at different θ first, and then a special θ with zero horizontal torque, denoted as θ_e, is sought as an equilibrium of ice crystal orientation. The equilibrium is classified into two kinds: stable and unstable. Ice crystals rotate to θ_e of stable equilibriums while deviating from θ_e of unstable ones once they are released into quiet air. Multiple equilibriums of ice crystal orientation are found via numerical simulations. A cylinder with D/L close to one has three equilibriums, two of which are stable (i.e., $\theta_e = 0°$ and 90°). A cylinder with D/L away from one has only two equilibriums, one of which is stable (i.e., either $\theta_e = 0°$ or 90°). In addition, an asymmetric cylinder has two, three, or five equilibriums, and their θ_e is sensitive to the distance between its geometrical center and its center of gravity. The sensitivity of θ_e to crystal asymmetry suggests large symmetric ice crystals tend to become asymmetric (or irregular) and subsequently oriented randomly.

SIGNIFICANCE STATEMENT: Ice crystal orientation impacts high-cloud reflectance and satellite-based observations of high clouds significantly. However, its laboratory and field observations look dissimilar: the percentage of horizontally oriented ice crystals (HOICs) observed in the laboratory is quite high, while in the field it is often low and varies greatly in space and time. The motivation for this study is to elucidate what causes the difference between the laboratory and field observations. The torque acting on ice crystals are computed by modeling the airflow around ice crystals, revealing the conditions for nonhorizontal orientations of ice crystals. In quiet air, an ice crystal is oriented either horizontally or vertically when its shape is close to sphere. When its shape is elongated in one direction, its orientation depends on its asymmetry in density and shape. The sensitivity of ice crystal orientation to ice crystal asymmetry explains the low percentage of HOICs in the field, because asymmetric ice crystals are common in clouds. As an application, this sensitivity together with the observed percentage of HOICs can be used to infer the processes of ice crystal growth in clouds, providing clues to better representation of ice crystals in weather and climate models.

KEYWORDS: Cirrus clouds; Ice crystals; Numerical analysis/modeling

1. Introduction

Ice crystal orientation plays an important role in the water and energy processes in the atmosphere, for example, via its effects on cloud albedo (Takano and Liou 1989; Zhou et al. 2012), ice crystal fall speed (Heymsfield and Iaquinta 2000), and precipitating ice crystal formation (Zeng et al. 2022). However, ice crystal orientation remains a puzzle because the results of laboratory and field observations differ. Jayaweera and Mason (1965) observed the orientation of cylinders as they fell in a tank containing liquid and found the dominance of horizontally oriented cylinders. This result was later confirmed by other laboratory experiments (e.g., Westbrook 2011). If the process leading to horizontal orientation was the only process determining ice crystal orientation, horizontally oriented ice crystals (HOICs) would dominate all ice clouds at all latitudes. However, the prediction of HOICs is contrary to field observations using a variety of different techniques: the percentage of HOICs is often low and varies greatly in space and time [Bréon and Dubrulle 2004; Noel and Chepfer 2010; Neely et al. 2013; Garrett et al. 2015; Goerke et al. 2017; Gong et al. 2018; Zeng et al. 2019, 2021; Kikuchi et al. 2021; see Zeng et al. (2022) for a review].

To understand the disparity in ice crystal orientation between the laboratory and field observations, we study the dynamics of ice crystal orientation first by modeling the airflow around ice crystals. Our model setup is like the previous ones (Hashino et al. 2014, 2016; Cheng et al. 2015; Tagliavini et al. 2021a,b) but aims at a hypothesis of multiple equilibriums of ice crystal orientation.

The hypothesis of multiple equilibriums of ice crystal orientation is schematized in Fig. 1. Consider a cylinder with diameter D and length L. It mimics a column- and plate-like ice crystal when $D/L < 1$ and >1, respectively. Its orientation is

Denotes content that is immediately available upon publication as open access.

Corresponding author: Xiping Zeng, xiping.zeng.civ@army.mil

DOI: 10.1175/JAS-D-22-0223.1

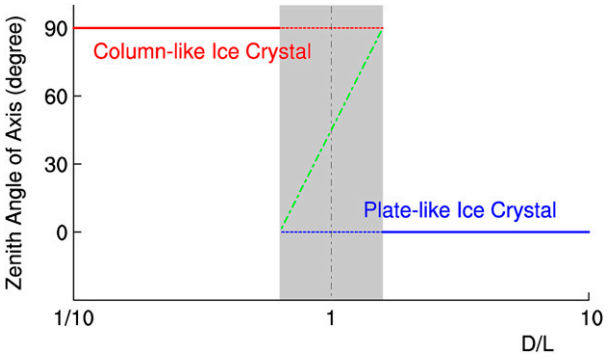

FIG. 1. Schematic of three equilibriums of cylinder orientation (shading). A cylinder with diameter D and length L, mimicking a column-like (red) and plate-like (blue) ice crystal when $D/L < 1$ and >1, respectively, is oriented with a zenith angle of axis at equilibrium (or $\theta = \theta_e$), which is shown by a line. Two solid lines represent two stable equilibriums that correspond to the laboratory-observed horizontal alignment of ice crystals; dashed lines are inferred based on the continuity of cylinder orientation against D/L. The green line represents an unstable equilibrium that is inferred for the separation of the two stable equilibriums.

described by θ the zenith angle of its axis. When it stays at a steady state aloft, its orientation is described by $\theta = \theta_e$, where $\theta_e = 0°$ and 90° for plate- and column-like types (or the solid lines in Fig. 1), respectively, based on the laboratory observations of cylinders and hexagonal columns (Jayaweera and Mason 1965; Westbrook 2011). Considering the continuity of the steady cylinder orientation θ_e against D/L, we hypothesize that an ice crystal has two stable equilibriums of cylinder orientation (i.e., $\theta_e = 0°$ and 90°) when $D/L \sim 1$. If the two stable equilibriums coexist, an unstable equilibrium must exist to separate them (see the green line in Fig. 1), which raises a new question on the regions of the three equilibriums as well as their factors (e.g., D/L). In addition, we hypothesize that an asymmetric ice crystal, whose geometrical center deviates from its center of gravity, has multiple stable orientations of $\theta_e \neq 0°$ and 90°.

To test the hypothesis of multiple equilibriums of ice crystal orientation, numerical simulations of airflow around cylinders are carried out and their results are reported in this paper. The paper consists of six sections. Section 2 introduces the numerical model used as well as its evaluation. Sections 3 and 4 present the model results for the multiple equilibriums of symmetric and asymmetric cylinders, respectively. Section 5 uses the multiple equilibriums to explain the difference in ice crystal orientation between the laboratory and field observations. Section 6 concludes.

2. Evaluation of the numerical model

A numerical model of airflow around solid objects (see appendix A) is used to simulate the torque acting on ice crystals aloft. It is introduced first in this section as well as appendix A, and then evaluated by comparing the modeled and observed drag force coefficients of solid spheres in the air.

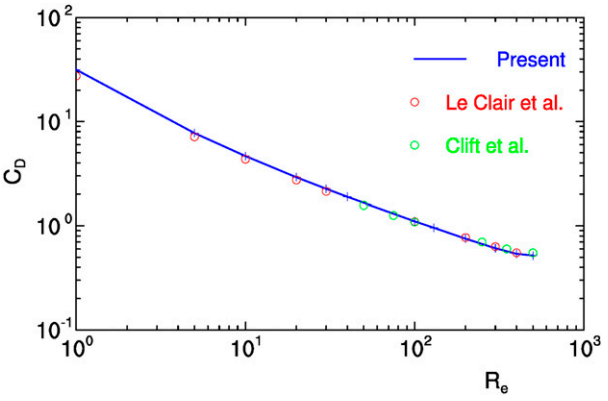

FIG. 2. Comparison between the modeled drag force coefficient C_D for spheres (blue) and the laboratory observations from Le Clair et al. (1970) (red) and Clift et al. (1978) (green) at different Reynolds numbers Re.

The model represents the momentum equation (or the Navier–Stokes equation) and the continuity equation of compressible air by

$$\partial_t \mathbf{v} + \rho \mathbf{q} \times \mathbf{v} + \nabla k = -\rho^{-1} \nabla p + \nu \nabla^2 \mathbf{v}, \quad (1)$$

$$\partial_t \rho + \nabla \cdot \rho \mathbf{v} = 0, \quad (2)$$

respectively, where ∂_t stands for the partial derivative with respect to time t, $\mathbf{v}$ the velocity vector, p the pressure, ν the kinematic viscosity, and ρ the mass density of air. In Eq. (1), $k \equiv y\mathbf{v} \cdot \mathbf{v}$ is the kinetic energy per unit mass and $\mathbf{q} \equiv \rho^{-1} \nabla \times \mathbf{v}$ vorticity divided by air density. The model connects the pressure and density by

$$\partial_t p = c_s^2 \partial_t \rho, \quad (3)$$

where c_s is the speed of sound waves. In this study large c_s (or small Mach number) is chosen so that the model can represent incompressible flow around solid objects.

The model is used to simulate a solid sphere with diameter D that is immersed in an environmental flow with mean velocity U_∞. The simulations are performed for Reynolds number $\mathrm{Re} = U_\infty D/\nu$ from 1 to 500 and the Mach number $M = c_s/U_\infty = 1.2 \times 10^{-3}$.

The model employs a stretched grid with fine resolution near the sphere in the domain center and coarse resolution near the lateral boundaries for a trade-off between domain center resolution and domain size. It uses $256 \times 256 \times 256$ grid points with the minimum grid size $\Delta x_{\min}$ (or $\Delta y_{\min}$, $\Delta z_{\min}$) $= D/41$. Its grid size of 30 layers near the lateral boundaries is increased from $\Delta x_{\min}$ at the innermost layer to $30\Delta x_{\min}$ at the outermost layer with a step of $\Delta x_{\min}$. In addition, the model uses a dimensionless time step $\Delta t U_\infty/D = 1 \times 10^{-4}$ for numerical integration.

The model is used to obtain the drag force coefficient C_D versus the Reynolds number. The modeled results are compared with their laboratory observations in Fig. 2, showing the model is accurate when $\mathrm{Re} < 500$ the maximum Reynolds number used in the present simulations.

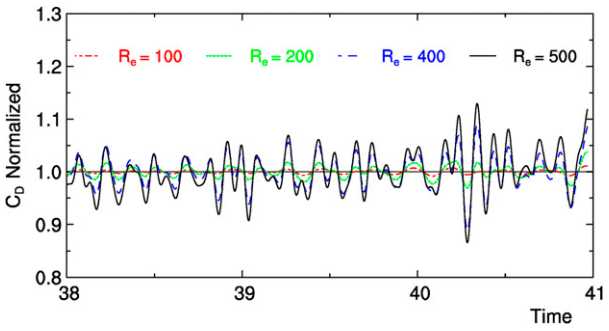

FIG. 3. Time series of the modeled drag force coefficient C_D for spheres at Re = 100 (red), 200 (green), 400 (blue), and 500 (black), where the coefficient is normalized by its mean time average between dimensionless times 38 and 41.

Figure 3 displays the time series of the modeled drag force coefficient C_D, exhibiting the fluctuation of C_D around its mean average, where the dimensionless time is defined as tU_∞/D. The fluctuation resembles the laboratory observations on "the onset of faint, periodic, pulsative motions downstream of the standing eddy" at Re > 100; the fluctuation becomes increasingly pronounced as Re increases, resembling the laboratory observations (Pruppacher and Klett 1997; Johnson and Patel 1999).

3. Multiple equilibriums of ice crystal orientation

In this section the numerical model is used to test the hypothesis of multiple equilibriums of cylinder orientation (see Fig. 1). To be specific, it is used to simulate the hydrodynamic torque acting on cylinders, focusing on the torque versus cylinder orientation.

a. Simulation setup

The model is set up as in Fig. 4. Consider a circular cylinder with two Cartesian coordinate systems. One coordinate system, (x, y, z), moves vertically with the cylinder. Its z axis points upward and its x axis is chosen so that the cylinder axis is in the x–z plane at $y = 0$. The other coordinate system, (x', y', z'), shares the same y axis with the first system and is rotated around the y axis until the z' axis is parallel to the axis of the cylinder.

The model is embodied in the latter coordinate system. Since the two coordinate systems share the same y axis, they share the same component of the torque T_y acting on the cylinder in the y-axis direction. In this study, T_y is computed first in the coordinate system (x', y', z'), and then used to explain the rotation of the cylinder in the coordinate system (x, y, z). To be specific, when $T_y < 0$, the cylinder rotates around the y axis to decrease θ the zenith angle of cylinder axis; when $T_y > 0$, the cylinder rotates to increase θ; when $T_y = 0$, the cylinder is at an equilibrium. *The present numerical experiments aim to find the conditions for $T_y = 0$.*

The cylinder is described by two variables: diameter D and length L. Its orientation is described by a third variable θ, the zenith angle of cylinder axis. Consider now a cylinder immersed in an environmental flow with mean velocity U_∞ (Fig. 4).[1] Air flows around the cylinder, which is simulated given the Reynolds number. Please note the Reynolds number $\mathrm{Re} = U_\infty D/\nu$ is defined for all cylinders (or crystals) for the sake of simplicity even when the environmental velocity is not perpendicular to the surface with diameter D. A real Reynolds number of a case is related to Re with the real characteristic length.

b. Stability analysis of cylinder orientation

Numerical simulations are carried out for five cylinder shapes: D/L = 1/2, 1/1.25, 1, 1.25, and 2. Given cylinder shape and orientation (or θ), the simulations are performed in turn with the Reynolds numbers Re = 40, 100, 200, and 400. All the simulations are set up as those in section 2 with 256 × 256 × 256 grid points, mimicking cylinders immersed in a wind tunnel with mean velocity U_∞.

The simulations run until they reach steady state. Their T_y at the steady state (or typically between dimensionless time 38 and 41) is displayed against θ in Fig. 5, where T_y is normalized by $\rho_a U_\infty^2 (0.5D)^3$ (Hashino et al. 2014). The sign of T_y is used to analyze the stability of cylinder orientation, which is illustrated with the results at Re = 100.

When Re = 100 and $D/L = 1$, there are three orientation equilibriums with $T_y = 0$: two stable equilibriums at $\theta = 0°$ and 90°, and an unstable one at $\theta = 36.5°$. If initial $\theta < 36.5°$, the cylinder rotates to $\theta_e = 0°$ eventually; if initial $\theta > 36.5°$, the cylinder rotates to $\theta_e = 90°$. Hence, the two equilibriums of $\theta_e = 0°$ and 90° are stable. Since θ never returns to 36.5° once deviating from 36.5°, the equilibrium of $\theta_e = 36.5°$ is unstable. In summary, $\theta_e = 0°$, 36.5°, and 90° represent the three orientation equilibriums of a cylinder with $D/L = 1$ at

[1] The terminal velocity of a crystal U_∞ is determined through the condition of balance between the gravitation force and the drag force acting on the crystal. Given crystal size, shape, and density, U_∞ can be known via numerical simulation (Hashino et al. 2014, 2016; Cheng et al. 2015; Tagliavini et al. 2021a,b). In this paper we take a new approach to decouple U_∞ and crystal orientation and then achieve a "simple" relationship between crystal shape and orientation (e.g., Fig. 6).

If an air parcel containing ice crystals has no horizontal acceleration, the ice crystals move horizontally with the parcel and thus do not move horizontally relative to the parcel. As a result, U_∞ is not related to the horizontal velocity of the parcel. If an air parcel undergoes horizontal acceleration caused by other processes, its crystals do move horizontally relative to the parcel, and thus, their orientations are changed by the acceleration. To represent the horizontal acceleration of the parcel, the z axis of the noninertial framework of a crystal in Fig. 4 is used to point in the opposite direction to the sum of the inertial and gravitation forces on the crystal, and the sum of the inertial and gravitation forces is balanced by the drag force acting on the crystal. When the z axis is not vertical, a stable equilibrium of $\theta_e = 0°$ (or 90°) corresponds to a canting mode where crystals align neither horizontally nor vertically.

The orientation of a stable equilibrium in the Earth framework, referred to here as a target orientation of a crystal, is related to both θ_e and the orientation of the z axis. Since turbulence and gravity waves change the orientation of the z axis, they change the target orientation. Hence, the effects of turbulence and gravity waves on crystal orientation can be described by a simple model: a crystal is always rotating to approach a varying target orientation.

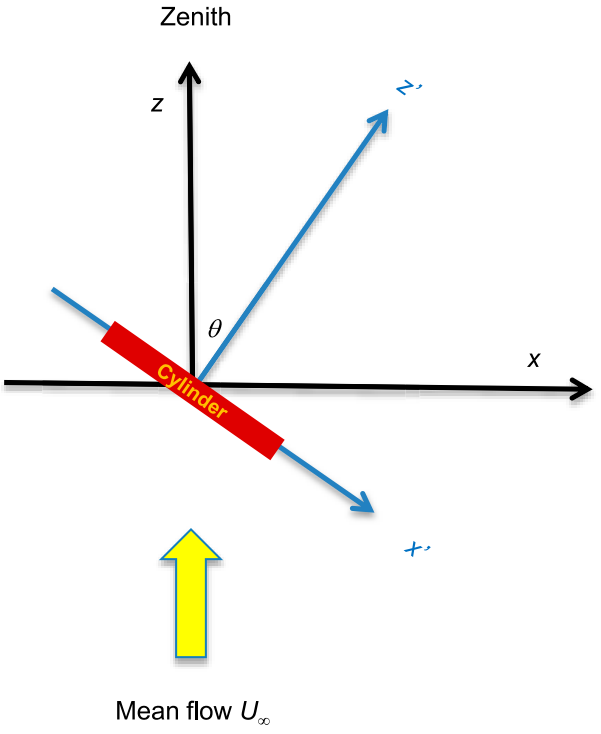

FIG. 4. Vertical cross section of the first Cartesian coordinate system (x, y, z) (black) that moves vertically with a cylinder (red) and the second Cartesian coordinate system (x', y', z') (blue) that is rotated around the y axis until the z' axis is parallel to the axis of the cylinder. The numerical model is embodied in the second coordinate system.

Re = 100. This result of Fig. 5 can be used to infer the orientation of ice crystals given Re or U_∞.[2]

The equilibriums vary with D/L. When Re = 100, there are only two equilibriums at D/L = 1/2 (column-like): a stable equilibrium of θ_e = 90° and an unstable one of θ_e = 0°, indicating that the cylinder rotates to θ_e = 90° eventually no matter what its initial θ is. In contrast, there are two different equilibriums at D/L = 2 (plate-like): a stable equilibrium of θ_e = 0° and an unstable one of θ_e = 90°, indicating that the cylinder rotates to θ = 0° eventually no matter what its initial θ is.

The equilibriums change with not only D/L but also Re. When Re = 100, there are three equilibriums at D/L = 1/1.25, 1, and 1.25, and two equilibriums at D/L = 1/2 and 2. In contrast, there are three equilibriums only at D/L = 1 when Re = 40 but at D/L = 1/2, 1/1.25, 1, 1.25, and 2 when Re = 400. This sensitivity of the equilibriums to Re is understandable, because Re changes the wake vortexes and thus T_y. In short, these modeling results in Fig. 5 support the hypothesis of multiple equilibriums

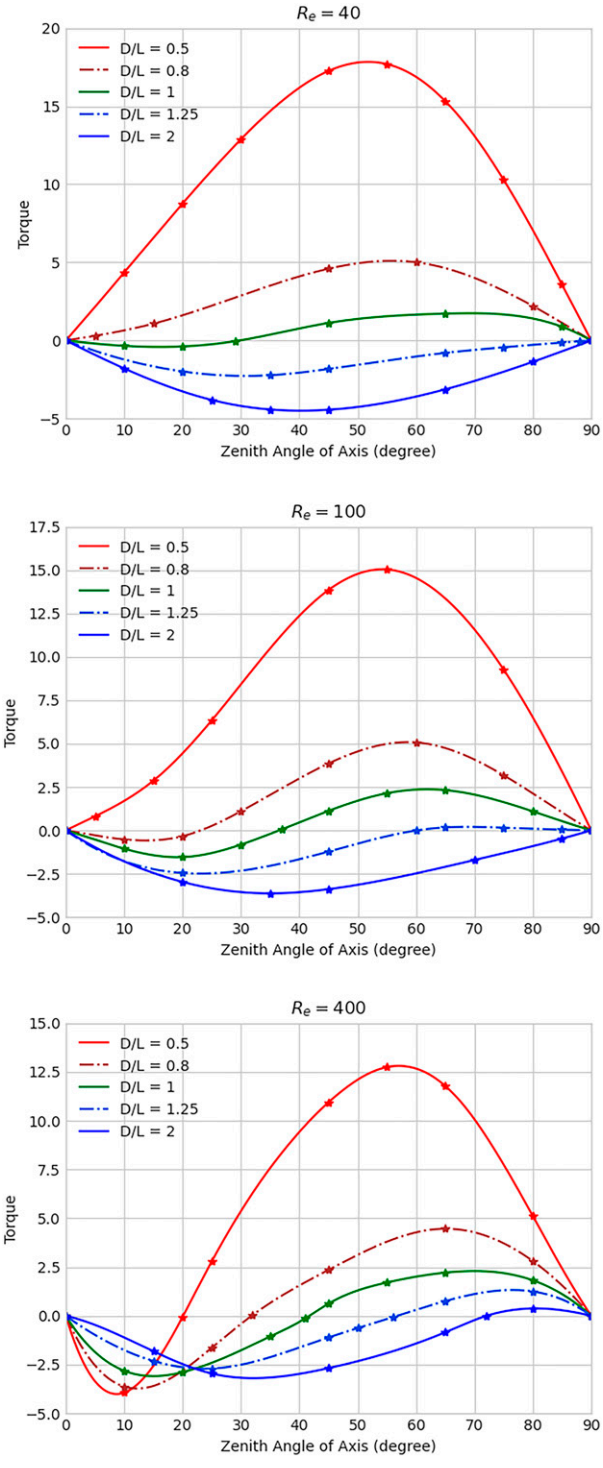

FIG. 5. Torque T_y acting on cylinders with diameter D and length L vs the zenith angle of cylinder axis θ when Re = (top) 40, (middle) 100, and (bottom) 400. A symbol corresponds to a numerical experiment. An equilibrium of cylinder orientation is described by θ with T_y = 0 (i.e., θ_e).

[2] Consider a column-like ice crystal with L =1020 μm, D/L = 0.2, and density = 0.34 g cm^{-3}. Thus, its terminal velocity U_∞ = 1 m s^{-1} and Re = 40 (Heymsfield and Iaquinta 2000). Using these parameters, the torque acting on the ice crystal and the orientation of the ice crystal can be estimated based on Figs. 5 and 6, respectively.

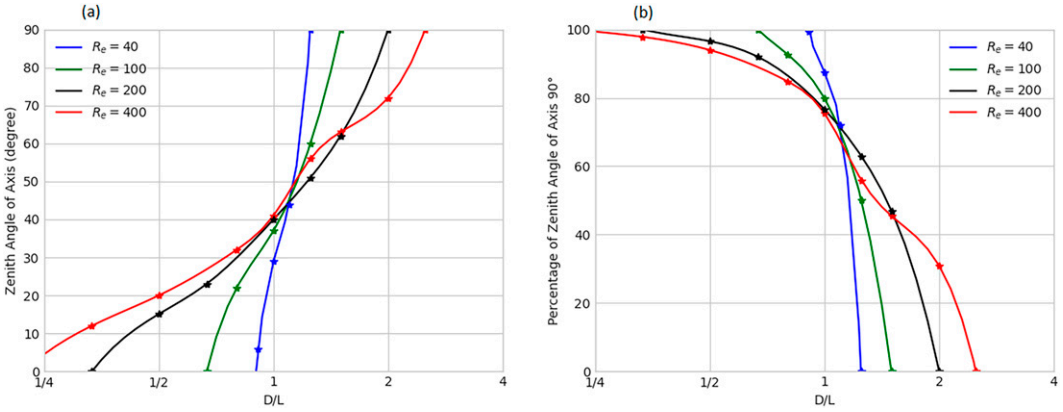

FIG. 6. (a) Steady-state zenith angle of cylinder axis at the unstable equilibrium θ_e vs D/L for cylinders with diameter D and length L. Symbols denote the results based on the numerical experiments (including those in Fig. 5). (b) Percentage of cylinders with the zenith angle of 90° if all the cylinders are initially released randomly into quiet air.

in Fig. 1, and show the conditions for multiple equilibriums vary with D/L and Re.

c. *Distribution of cylinder orientations in quiet air*

The equilibriums determine the orientation of cylinders in quiet air. Specifically, the zenith angle of crystal axis at unstable equilibrium θ_e determines the distribution of cylinder orientations. Suppose, for example, that many cylinders with the same size, shape ($D/L = 1$), and Re = 100 are released randomly in two (zenith and azimuth angles) dimensions into quiet air (with neither turbulence nor gravity waves). Since the cylinders possess an unstable equilibrium of $\theta_e = 36.5°$, those with initial $\theta < 36.5°$ rotate eventually to the stable equilibrium at $\theta_e = 0°$ while the remainder, with initial $\theta > 36.5°$, rotate to the stable equilibrium at $\theta_e = 90°$. As a result, a proportion of the cylinders reaches their steady state with orientation $\theta = 0°$, whereas the remainder reaches their steady state with orientation $\theta = 90°$. The percentage of cylinders with orientation $\theta = 90°$ is equal to $\cos\theta_e = 80.4\%$; the percentage of cylinders with orientation $\theta = 0°$, $(1 - \cos\theta_e) = 19.6\%$.

Since θ_e of unstable equilibrium varies with D/L and Re, the numerical experiments in Fig. 5 as well as additional ones are used to obtain θ_e of unstable equilibrium at different D/L and Re. Figure 6a displays θ_e of unstable equilibrium against D/L at different Re. Generally speaking, θ_e of thin disks ($D/L \gg 1$) at the unstable equilibrium $\approx 90°$ and θ_e of long column (or $D/L \ll 1$) approaches 0° but is still >0° at relatively high Reynolds numbers.

The percentage of cylinders with the steady-state zenith angle $\theta = 90°$, determined from θ_e of unstable equilibrium, is displayed in Fig. 6b. When $D/L \ll 1$, the percentage of long column with $\theta = 90°$ is close to 100% (i.e., most long columns are horizontally oriented, while a small proportion is vertically oriented especially at relatively high Reynolds number). In contrast, for thin disks ($D/L \gg 1$) there is no unstable equilibrium between 0° and 90°. Thus, the percentage of thin disks with $\theta = 0°$ is close to 100%, or almost all thin disks are horizontally oriented. These results are consistent with the laboratory observations of Jayaweera and Mason (1965) and Westbrook (2011).

4. Orientation of asymmetric cylinders

As shown in section 3, symmetric thin disks have a stable equilibrium of $\theta_e = 0°$; long columns, $\theta_e = 90°$. In this section, the numerical model is used to study the sensitivity of stable equilibrium to cylinder asymmetry and show asymmetric cylinders possess $\theta_e \neq 0$ and 90°.

a. *Disk simulations*

Consider a cylinder with $D/L = 4$ (i.e., a disk). It is assumed to be asymmetric in density so that its mass center deviates from its geometrical center. Let d denote the distance between the mass center and the geometrical center. Thus, d/D measures its asymmetry. Hence, the torque acting on the cylinder with respect to the mass center, instead of the geometrical center, varies with d/D.

To simulate the flow around the cylinder accurately, $1024 \times 512 \times 1024$ grid points are used and the minimum grid size $\Delta x_{\min} = D/161$ is set. The grid size at the 60 layers near the lateral boundaries is increased from $\Delta x_{\min}$ at the innermost layer to $60\Delta x_{\min}$ at the outermost layer with a step of $\Delta x_{\min}$, providing a large domain to accommodate the flow around the cylinder. In addition, the mass center of the cylinder is located at $(d, 0, 0)$ in the coordinate system (x', y', z').

Suppose, for example, the cylinder is oriented with a zenith angle of axis $\theta = 10°$. Two simulations are carried out, with Re = 100 and 400. Modeled streamlines for these cases at $y = 0$ and dimensionless time $t = 36.82$ is displayed in Fig. 7, showing that the two vortexes behind the cylinder are not symmetric. Clearly the asymmetry between the two wake vortexes is stronger at Re = 400 than at Re = 100.

The modeled torque at the steady state (specially, its average over time 36.1 to 36.8) is displayed against d/D in Fig. 8a. The torque equals zero at $d/D = 0.0492$ when Re = 100 and at $d/D = 0.0273$ when Re = 400. In other words, a cylinder

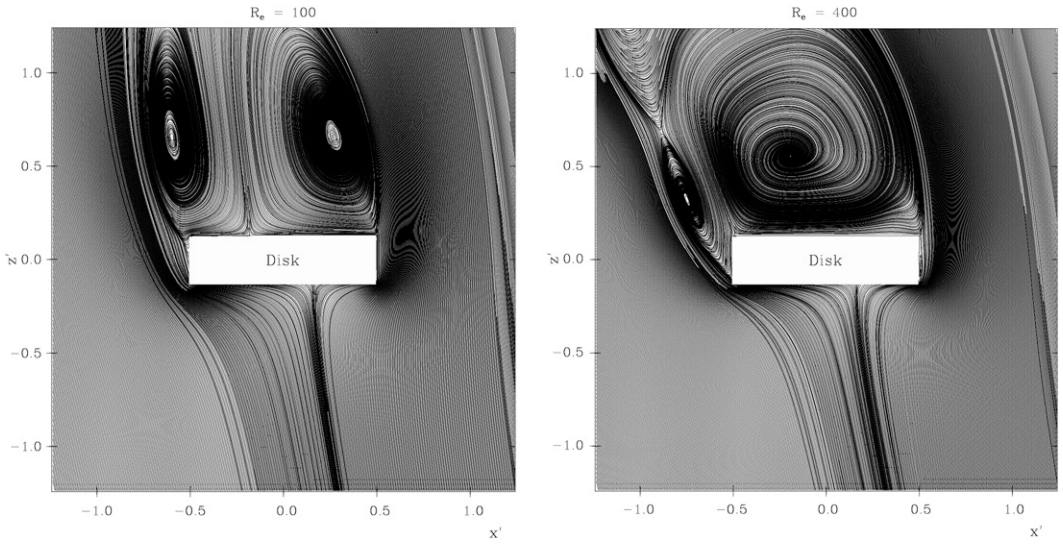

FIG. 7. Vertical cross section of streamlines around a disk at $y = 0$ and $t = 36.82$ with Re = (left) 100 and (right) 400, where $D/L = 4$ and $\theta = 10°$. The horizontal and vertical axes are normalized by the disk diameter D.

with $d/D = 0.0492$ has an equilibrium of $\theta_e = 10°$ when Re = 100, and another cylinder with $d/D = 0.0273$ has an equilibrium with the same θ_e when Re = 400. This sensitivity of cylinder orientation to Re is understandable. Consider a cylinder with $d/D = 0.0492$. Its $T_y = 0$ at Re = 100 but $T_y > 0$ at Re = 400 (see Fig. 8a), showing that the strong asymmetry between two wake vortexes at Re = 400, in contrast to that at Re = 100 (Fig. 7), tends to drive the cylinder away from horizontal alignment.

Figure 8b shows that the distance between the mass center and the geometrical center that maintains zero torque fluctuates slightly at Re = 400 but very little at Re = 100, indicating that the shedding of eddies from the rear of falling cylinders impacts cylinder orientation slightly. This weak effect of eddy shedding on cylinder orientation resembles to some extent the influence of eddy shedding on drag coefficient for spheres, seen in Fig. 3. The weak effect is understandable because faint and pulsative motions downstream of the standing eddy occur only for large Re.

To quantify the sensitivity of cylinder orientation to asymmetry, many numerical simulations with different cylinder orientation (or θ) are carried out, and the torque modeled for a range of asymmetry levels is displayed against θ in Fig. 9a. The green line in Fig. 9a, for example, for a cylinder with $d/D = 0.12$ versus θ shows that the torque equals zero at $\theta = 74.5°$ and 90°. Since $T_y > 0$ ($T_y < 0$) when $\theta < 74.5°$ ($\theta > 74.5°$), the cylinder with $d/D = 0.12$ rotates to $\theta_e = 74.5°$ eventually, assuming its initial $\theta < 90°$. Hence, the equilibrium of $\theta_e = 74.5°$ is stable and the one at $\theta_e = 90°$ is unstable.

Similar analysis is performed to obtain θ_e of the stable equilibrium with other d/D. Figure 9b displays the θ_e of the stable equilibrium against d/D, showing that θ_e increases significantly with asymmetry especially near $d/D = 0.1$. Clearly $0° < \theta_e < 90°$ at the stable equilibrium where the hydrodynamic force and gravity

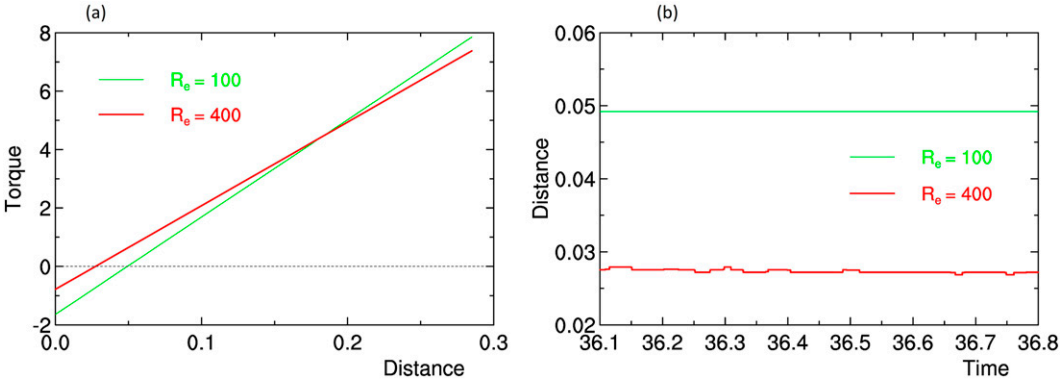

FIG. 8. (a) Torque acting on a cylinder (averaged over times 36.1 and 36.8) vs the dimensionless distance between the mass center and the geometrical center. (b) The distance for zero torque vs time, where $D/L = 4$ and $\theta = 10°$ with Re = 100 (green) and 400 (red).

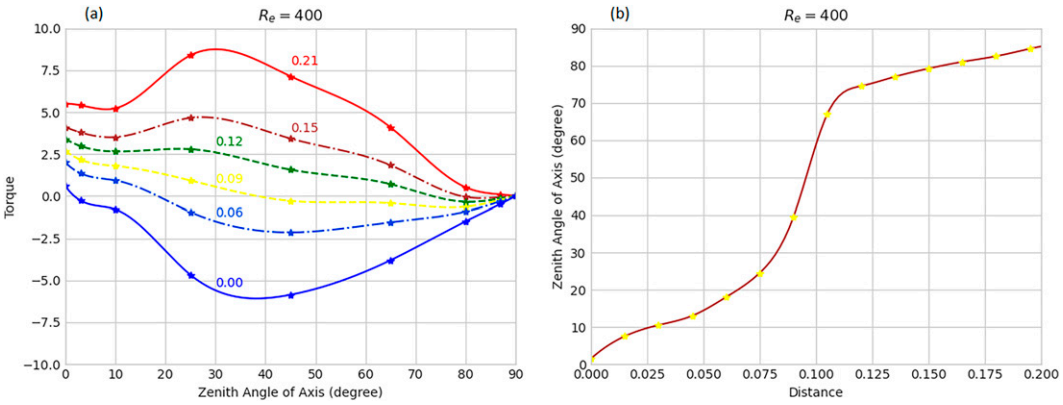

FIG. 9. (a) Torque acting on asymmetric cylinders with $D/L = 4$ (i.e., a disk) at Re = 400 (averaged over the time interval from 36.1 to 36.8) vs the zenith angle of cylinder axis given the dimensionless distance d/D between the mass center and the geometrical center (numbers beside lines). (b) The zenith angle of cylinder axis at zero torque vs the dimensionless distance (asymmetry).

reaches balance. In other words, *disks with mass asymmetry are oriented neither horizontally nor vertically*.

b. Column simulations

Consider a cylinder with $D/L = 1/4$ (i.e., a column). Unlike for the thin disk, its mass center is located at cylinder axis. In the present simulations, its mass center is located at $(0, 0, -d)$ in the coordinate system (x', y', z') so that θ_e falls in $[0°, 90°]$ (the setup with the mass center at $(0, 0, d)$ brings about no new information because of the symmetry between $(0, 0, -d)$ and $(0, 0, d)$ except that θ_e fall in $[90°, 180°]$).

The simulations are set up as those in the preceding subsection, also using $1024 \times 512 \times 1024$ grid points. Their minimum grid size $\Delta x_{\min} = D/161$ is set so that the flow around the edge of the cylinder is resolved with sufficient grid points. The simulations use Re = 400 and different cylinder orientation (or θ). The computed torque is displayed against θ in Fig. 10a.

The torque acting on a column is quite different from that on a disk. The green line in Fig. 10a, for example, shows that the cylinder with $d/D = 0.12$ has three equilibriums: two stable ones of $\theta_e = 0°$ and 84.5°, and an unstable one of $\theta_e = 8°$. If its initial $\theta < 8°$, the cylinder rotates to $\theta_e = 0°$; otherwise, the cylinder rotates to $\theta_e = 84.5°$. In contrast, the purple line in Fig. 10a shows that the cylinder with $d/D = 0.27$ has five equilibriums: three stable ones of $\theta_e = 0°$, 37°, and 73°, two unstable ones at $\theta_e = 10°$ and 46°. If its initial $\theta < 10°$, the cylinder rotates to $\theta_e = 0°$; for initial θ between 10° and 46°, to $\theta_e = 37°$; for initial $\theta > 46°$, to $\theta_e = 73°$.

Figure 10b uses purple and blue lines to denote θ_e of, respectively, stable and unstable equilibriums as a function of the asymmetry d/D. In other words, the blue lines divide the plane into several regions so that an initial point in a region (or the initial status of cylinder) will travel toward a stable equilibrium (or purple line) while deviating from an unstable one. When $d/D < 0.25$, a cylinder above the lower blue line travels toward the upper purple line; below the lower blue line, toward the lower purple line. When $d/D > 0.25$, an initial status of cylinder above the upper blue line travels toward the upper purple line; between the two blue lines, toward the middle purple line; below the lower blue line, toward the lower purple line. Hence,

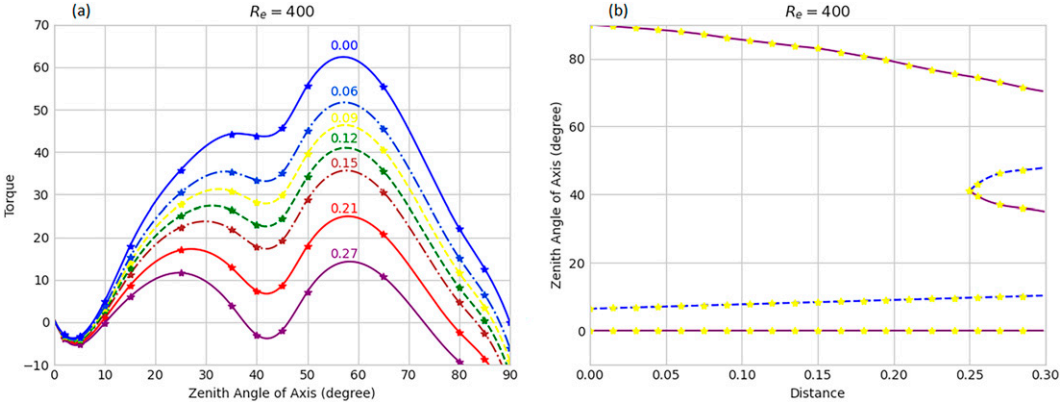

FIG. 10. As in Fig. 9, but for a cylinder with $D/L = 1/4$ (i.e., a column) computed for Re = 400. In (b), Purple and blue lines represent stable and unstable equilibriums, respectively, vs the dimensionless distance (asymmetry).

the final, steady-state orientation of asymmetric columns is quite sensitive to d/D.

If asymmetric columns are released with random orientation into quiet air, they rotate eventually to the orientations of their two (or three) stable equilibriums (represented by the purple lines in Fig. 10b). The percentages of ice crystals with different orientations depend on the locations of the unstable equilibriums that are represented by the blue lines in Fig. 10b. Roughly speaking, when $d/D < 0.25$, the percentage of columns with vertical orientation (or $\theta = 0°$) is ~1.5%, whereas the percentage of columns with approximately horizontal orientation (or $\theta \approx 85°$) is ~98.5%; when $d/D > 0.25$, the columns with three final orientations of $\theta \approx 0°$, 35°, and 75° have percentages of ~1.8%, 27.5%, and 70.7%, respectively. This modeled sensitivity of equilibrium to d/D is consistent with the modeled sensitivity of orientation in Hashino et al. (2016), to some extent. The three stable equilibriums explain the observations of Garrett et al. (2015) that asymmetric particles (e.g., aggregates, moderately rimed particles, and graupel) have a much broader range of orientation angles.

Since the stable equilibrium of the top purple line in Fig. 10b has $\theta_e \approx 80°$, it is referred to as the horizontal mode of column orientation. The horizontal mode has high probability (~98.5%), which agrees with the field observations of Kajikawa (1976). In contrast, the stable equilibrium of the bottom purple line in Fig. 10b has $\theta_e = 0°$, and it is referred to as the vertical mode of column orientation. The vertical mode has low probability (~1.5%), which agrees with the observations of Zikmunda and Vali (1972) that some of the *rimed* crystals fell with their major axis vertical.

5. Discussion

We postulate that the difference in ice crystal orientation between the laboratory and field observations can be explained by two contributing factors: 1) the difference in turbulence and gravity waves between the laboratory and the field and 2) the difference between the very symmetric crystal models used in the laboratory and the asymmetric crystals formed in clouds (Kajikawa 1992), which are discussed below in turn.

a. *Effects of turbulence and gravity waves*

The effect of turbulence on crystal orientation is usually studied by modeling spheroids in turbulent air. Since spheroids approach a stable equilibrium or a target orientation in quiet air, turbulence leads to the random orientation of spheroids by changing the acceleration of air and subsequently interrupting the approach of spheroids to their target orientation (Cox 1965; Klett 1995; Siewert et al. 2014). However, ice crystals in clouds are more complicated than spheroids because of their sharp edges and asymmetry. Ice crystals with sharp edge and asymmetry usually have multiple stable and unstable equilibriums, and consequently, their orientations depend on their initial orientations in quiet air (see section 3). In turbulent air, turbulence drives the target orientation of ice crystals from one stable equilibrium to another, bringing about the random orientation of ice crystals, which explains the broad range of orientation angles of asymmetric particles (e.g., aggregates, moderately rimed particles, and graupel) observed by Garrett et al. (2015).

Turbulence is strong in convective regions, and its effect on crystal orientation is observed (Garrett et al. 2015; Zeng et al. 2019). In contrast, turbulence is weak or virtually nonexistent in thin cirrus clouds with high static stability (Zeng et al. 2020). Hence, the random distribution of crystal orientation observed in thin clouds (Noel and Chepfer 2010; Kikuchi et al. 2021) can be attributed to gravity waves, because gravity waves can switch crystal target orientation between stable equilibriums, too.

In nature, both turbulence and gravity waves contribute to the low frequency of HOICs observed in optically thin ice cloud layers (Noel and Chepfer 2010; Kikuchi et al. 2021). In thin cirrus clouds, ice crystals are small, and thus, their aspect ratio (or D/L) tends to be close to one (Auer and Veal 1970). As a result, prismatic ice crystals possess an unstable equilibrium of orientation and two stable ones (i.e., the vertical and horizontal modes of crystal orientation). Since gravity waves and/or turbulent eddies frequently alter the slope of streamlines of the environmental airflow around ice crystals (or the direction of mean flow U_∞ in Fig. 4; see footnote 1), *ice crystal orientation swings frequently across the unstable equilibrium, and thus, its target alternates between the two stable equilibriums*, bringing about the observed random orientation of ice crystals.

b. *High frequency of irregular ice crystals*

The stable equilibrium of ice crystal orientation can be used to (partly) explain the irregular (or asymmetric) ice crystals commonly observed in the field (Heymsfield et al. 2002; Heymsfield and Miloshevich 2003; Stoelinga et al. 2007) and laboratory (Bailey and Hallett 2004). Consider an asymmetric ice crystal with distance d between the geometrical center and the center of gravity. It stays at a stable equilibrium with axis zenith angle θ_e. Since the gradient of water vapor near the upstream crystal surface is larger than that near the downstream crystal surface (Ji and Wang 1999; also see Fig. 7), water vapor deposits more near the upstream surface than near the downstream surface, increasing d. Once d is increased, θ_e of the stable equilibrium is increased (see Fig. 9b), working as positive feedback between d and θ_e.

The positive feedback between d and θ_e intensifies the asymmetry of disk-like ice crystals. Furthermore, θ_e increases rapidly from 30° at $d/D = 0.08$ to 75° at $d/D = 0.12$ (Fig. 9b). This marked increase of θ_e with d corresponds to strong feedback that may in turn lead to the onset of irregular ice crystals observed in the laboratory (Bailey and Hallett 2004) via the large gradient of water vapor near the upstream crystal surface.

Similarly, the positive feedback between d and θ_e works for column-like ice crystals via the dependence shown by the top purple line in Fig. 10b. When $d/D < 0.25$ (or $d/L < 0.0625$), the top purple line represents the stable equilibrium with high probability of ~98.5% and axis zenith angle $\theta_e = ~80°$ (or the horizontal mode); the bottom purple line represents the stable

equilibrium with low probability of ~1.5% and axis zenith angle $\theta_e = 0°$ (or the vertical mode, which is unimportant due to its low probability). When $d/D > 0.25$ (or $d/L > 0.0625$), the pattern of column orientation becomes complicated: the third stable equilibrium (or canting mode of column orientation) occurs with moderate probability of ~27.5% and axis zenith angle θ_e = ~38°. The onset of the third stable equilibrium may correspond to the onset of large asymmetric rosette ice crystals observed (Heymsfield et al. 2002).

c. *Application of the equilibrium conditions*

The probability distribution function (PDF) of ice crystal orientation is an important factor in the weather prediction models and remote sensing retrievals. It can be obtained from the Lagrangian and Eulerian frameworks in phase space (e.g., Fig. 10b). Theoretically, the two frameworks are equivalent but have different advantages when calculating the PDF.

In the Lagrangian framework, ice crystal orientation is studied by tracking individual ice crystals or tracking the movement of a point in phase space (e.g., Fig. 10b). Its time series provides sufficient information to diagnose alignment mechanisms. Since ice crystal orientation varies greatly with many factors (e.g., crystal shape, length, aspect ratio, density, and asymmetry; air density; turbulence, gravity waves), how to classify the orientation and then obtain its PDF is still a challenge.

In contrast, in the Eulerian framework, ice crystal orientation is studied by analyzing the distribution of equilibriums in phase space (e.g., lines in Fig. 10b) and the limit cycle in phase space [the limit cycle corresponds to the spiral falling mode of ice crystals in physics space but is not discussed in this paper; see Zeng (2023) for an example on the difference in phase space between the Lagrangian and Eulerian frameworks]. Its PDF can be obtained "easily." Consider, for example, symmetric disks with $D/L > 1.5$ and Re = 100. Since the disks have only one stable equilibrium of $\theta_e = 0°$, we assume that the disks align horizontally no matter how they are introduced into the atmosphere, even while they flutter around $\theta = 0°$ (Cheng et al. 2015; Nettesheim and Wang 2018).

Turbulence and gravity waves also impact the PDF of crystal orientation, which is illustrated using the columns with $D/L = 1$ and Re = 100. Consider an ideal atmosphere with neither turbulence nor gravity waves. Suppose the columns are released randomly in two (zenith and azimuth angles) dimensions into the atmosphere. Their PDF is dominated by two orientations: horizontal orientation with frequency 20% and vertical one with frequency 80%, because the columns have two stable equilibriums (Fig. 6b). If turbulence and/or gravity waves are introduced into the atmosphere, they alter the crystal orientation relative to the critical orientation of the unstable equilibrium θ_e. As a result, the crystals are always swinging between the two stable orientations, bringing about a random distribution of crystal orientation (see footnote 1 for a general discussion).

Clearly, the PDF of crystal orientation varies with crystal types. Consider, for example, a mixture of small columns with $D/L \sim 1$ and large symmetric disks in a cloud with weak turbulence. Thus, the PDF is relatively complicated: the small columns are oriented randomly, whereas the large disks are oriented horizontally. Once turbulence in the cloud becomes strong (e.g., in a convective region), all crystals are orientated randomly. Suppose we know the equilibriums of all types of crystals and the percentage of each crystal type in a cloud. We thus can obtain the PDF of crystal orientation in the cloud by considering the PDF of each crystal type first and then merging the PDFs of all the crystal types.

The present paper focuses on the equilibriums of cylinders that mimic plates, columns, and needles for the sake of simplicity. As a complement, appendix B deals with the equilibriums of hexagonal columns for a secondary orientation. With the same procedure, we can get the equilibriums of less regular crystals (e.g., scalene crystals) and then analyze their preferred orientations. If some irregular crystals have no equilibrium, it is inferred that they are oriented randomly.

Also, the PDF of crystal orientation would vary from cloud to cloud because crystal shape and symmetry interact with crystal orientation (e.g., crystals aggregate). One example is the positive feedback between column asymmetry and orientation that can bring about the canting and vertical orientations of columns and even irregular crystals (see section 5b). Hence, it cannot be assumed that ice crystals are horizontally orientated in all clouds (Ryzhkov et al. 2011).

6. Conclusions

Equilibriums of ice crystal orientation, described by the cylinder axis zenith angle θ_e, are analyzed by modeling the airflow around ice crystals. They are classified into two kinds: stable and unstable. In quiet air an ice crystal rotates away from its unstable equilibrium, and its orientation then approaches to θ_e of a stable equilibrium potentially oscillating around its value (Hashino et al. 2014, 2016; Cheng et al. 2015). If ice crystals are released randomly into quiet air, they eventually assume orientations of their stable equilibriums. In contrast, in clouds turbulent eddies and gravity waves alter the slope of streamlines of environmental flow around ice crystals that in turn changes θ_e (or orientation target). As a result, an ice crystal always pursues its varying orientation target but cannot arrive at a steady-state orientation, which is consistent with the observed fluttering of ice crystals around the horizontal plane (e.g., Kajikawa 1976; Noel and Sassen 2005; Goerke et al. 2017).

The numerical simulations reveal the multiple equilibriums of ice crystal orientation. The presence of the equilibriums helps to understand the ice crystal orientations observed in the field as follows.

- When $D/L \ll 1$ or $D/L \gg 1$, an ice crystal possesses two equilibriums, one of which is stable and the other is unstable ($\theta_e = 0°$ or 90°). The stable equilibrium corresponds to the horizontal orientation of ice crystals in quiet air, which is consistent with the laboratory observations of Jayaweera and Mason (1965) and Westbrook (2011).

- When D/L is close to one, an ice crystal possesses three equilibriums, two of which are stable. In clouds gravity waves and/or turbulent eddies alter the slope of streamlines of the environmental air flow around ice crystals. As a result, a small ice crystal can swing its orientation frequently across its unstable equilibrium, alternating its orientation target between the two stable equilibriums and thus bringing about random orientations of ice crystals, which is consistent with the low frequency of HOICs observed in optically thin ice cloud layers (Noel and Chepfer 2010; Zhou et al. 2012; Kikuchi et al. 2021).
- When a large ice crystal is asymmetric in mass density, θ_e of stable equilibrium falls between 0° and 90°. The asymmetry-induced change of θ_e is directly proportional to the distance d between the geometrical center and the center of mass. The positive relationship between θ_e and d can be used to explain the common asymmetric ice crystals observed in the atmosphere (Heymsfield et al. 2002; Heymsfield and Miloshevich 2003; Stoelinga et al. 2007).

The present paper focuses only on the flow dynamic factors of orientation of prismatic ice crystals. It must be noted that other factors are present, such as ice crystal habit (Magono and Lee 1966; Bailey and Hallett 2004) and the radiative effect on microphysics (Zeng et al. 2022), that are responsible for other characteristics of observed ice crystal orientation.

Acknowledgments. This research was supported by DoD High Performance Computing (HPC) for providing the computational resources used. The authors greatly appreciated two anonymous reviewers for their constructive comments.

Data availability statement. No datasets were generated or analyzed during the current study.

APPENDIX A

Structure of the Numerical Model

The numerical model was developed based on Zeng (2001). It was embodied in the Cartesian coordinate system (x, y, z). Since $\mathbf{v} = (u, v, w)$ and $\mathbf{q} = (q_x, q_y, q_z)$ in the coordinate system, Eqs. (1) and (2) are rewritten as

$$\partial_t u - (\partial_t u)^{(z)} - (\partial_t u)^{(y)} + \partial_x k = -\rho^{-1}\partial_x p + \nu(\partial^2_{xx}u + \partial^2_{yy}u + \partial^2_{zz}u), \tag{A1}$$

$$\partial_t v - (\partial_t v)^{(z)} - (\partial_t v)^{(x)} + \partial_y k = -\rho^{-1}\partial_y p + \nu(\partial^2_{xx}v + \partial^2_{yy}v + \partial^2_{zz}v), \tag{A2}$$

$$\partial_t w - (\partial_t w)^{(y)} - (\partial_t w)^{(x)} + \partial_z k = -\rho^{-1}\partial_z p + \nu(\partial^2_{xx}w + \partial^2_{yy}w + \partial^2_{zz}w), \tag{A3}$$

$$\partial_t \rho = \frac{1}{2}[(\partial_t \rho)^{(x)} + (\partial_t \rho)^{(y)} + (\partial_t \rho)^{(z)}], \tag{A4}$$

where three sets of symbols with superscript x, y, and z are defined as

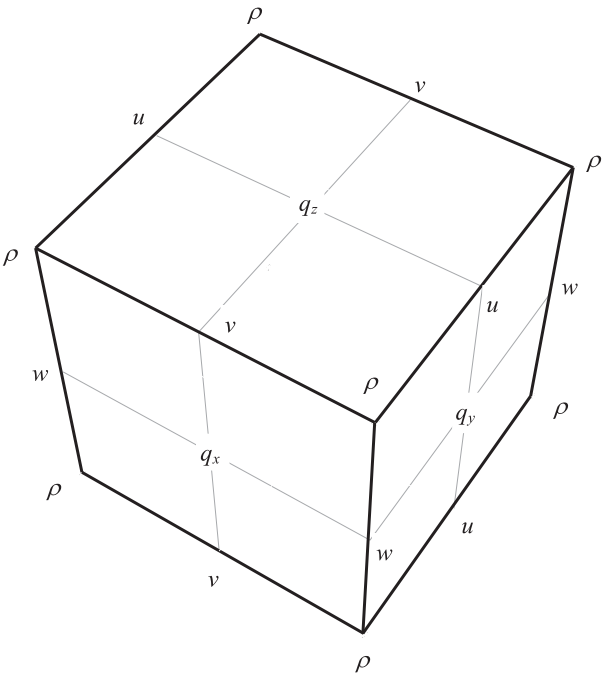

FIG. A1. Staggering of the variables (i.e., u, v, w, q_x, q_y, q_z, and ρ) in one cell of the numerical model. Pressure p and kinetic energy k are located at the same place as density ρ.

$$\left.\begin{aligned}(\partial_t v)^{(x)} - \rho w q_x &= 0\\ (\partial_t w)^{(x)} + \rho v q_x &= 0\\ (\partial_t \rho)^{(x)} + \partial_y \rho v + \partial_z \rho w &= 0\end{aligned}\right\}, \tag{A5}$$

$$\left.\begin{aligned}(\partial_t w)^{(y)} - \rho u q_y &= 0\\ (\partial_t u)^{(y)} + \rho w q_y &= 0\\ (\partial_t \rho)^{(y)} + \partial_z \rho w + \partial_x \rho u &= 0\end{aligned}\right\}, \tag{A6}$$

$$\left.\begin{aligned}(\partial_t u)^{(z)} - \rho v q_z &= 0\\ (\partial_t v)^{(z)} + \rho u q_z &= 0\\ (\partial_t \rho)^{(z)} + \partial_x \rho u + \partial_y \rho v &= 0\end{aligned}\right\}. \tag{A7}$$

Obviously, Eqs. (A5)–(A7) describe "two-dimensional flow" on the three planes y–z, z–x, and x–y, respectively, where their superscripts (i.e., x, y, and z) indicate the normal axes of the three planes, respectively. Please note (A5)–(A7) are still three-dimensional even though they look two-dimensional.

On the staggered grid in Fig. A1, the two-dimensional numerical scheme of Arakawa and Lamb (1981) is extended to (A5)–(A7), yielding a three-dimensional model (or the present one). The three-dimensional model converses not only kinetic energy $\mathbf{v} \cdot \mathbf{v}/2$ but also enstrophy $\mathbf{q} \cdot \mathbf{q}/2$ when $\nu = 0$ (for inviscid flow), which is unique as far as the authors are aware.

Since the model conserves both energy and enstrophy, it restrains the spurious energy cascade [see Zeng et al. (2020) for the discussion of enstrophy conservation and energy cascade]. As a result, the model possesses low computational noise and thus needs no artificial smoothing technique to maintain its

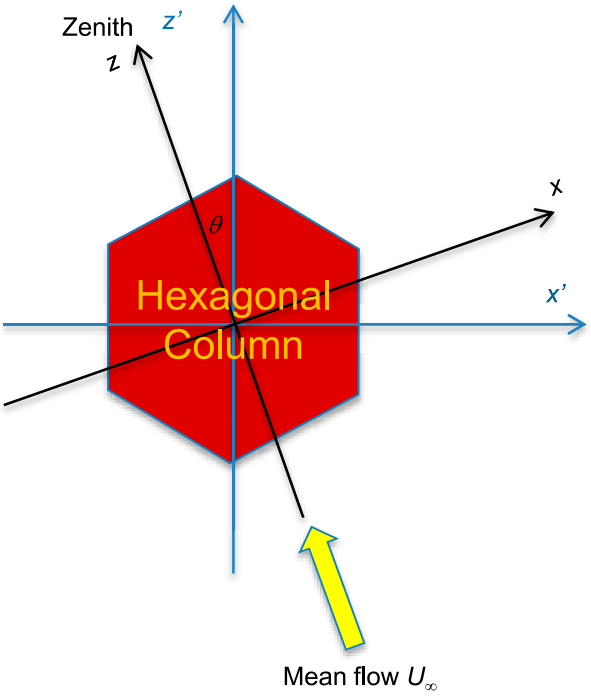

FIG. B1. As in Fig. 4, but for a hexagonal column with central axis aligned along the y axis.

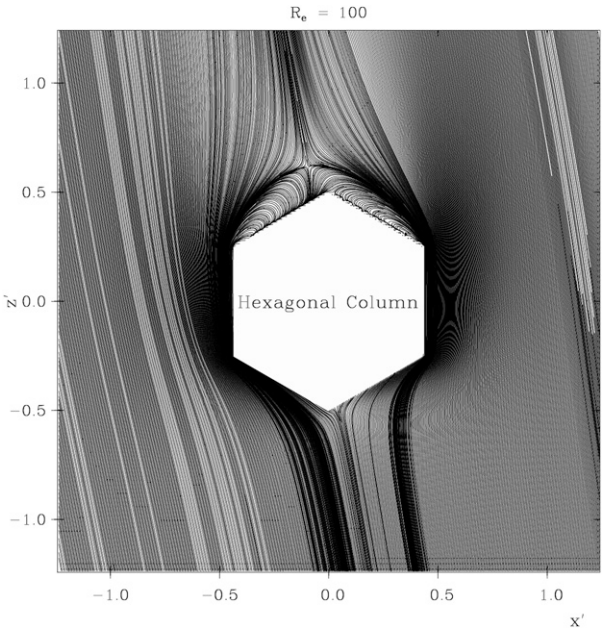

FIG. B2. Vertical cross section of streamlines around a hexagonal column at $y = 0$ and $t = 36.8$ with Re = 100, $L/D = 4$, and $\theta = 10°$. The horizontal and vertical axes are normalized by column diameter D. The small wake vortexes around the y axis in this figure are different from the large ones around the x axis (or the direction perpendicular to the central axis), since the former and latter wake vortexes are associated with the secondary and primary orientations, respectively.

computational stability. In addition, the model is accurate, which is shown by comparing the modeled and observed wake vortexes past solid cylinders and spheres (Zeng 2001; also see section 2).

The model is also tested by comparing the computed equilibrium of crystal rotation with the hexagonal column orientation observed. In section 3, the computed equilibrium for the primary orientation of cylinders is consistent with the horizontal alignment of crystals observed by Jayaweera and Mason (1965) and Westbrook (2011). In appendix B, the equilibrium for the secondary orientation of hexagonal columns is also consistent with the laboratory observations of hexagonal column orientation (Westbrook 2011).

APPENDIX B

Secondary Orientation of Hexagonal Columns

Section 3c shows the primary orientation of symmetric circular columns, in which their central axis aligns horizontally. As a complement, this appendix shows the secondary orientation of hexagonal columns by analyzing their other equilibriums. Figure B1 displays the model setup where the central axis of hexagonal columns is aligned along the y axis. All the simulations of hexagonal columns take the same gridding as the simulations in section 4b, using 1024 × 512 × 1024 grid points.

The first simulation is for a hexagonal column with $L/D = 4$, $\theta = 10°$, and Re = 100. The column arrives at its steady status in dimensionless time ~30 and the steady status is described with the variables averaged between time 36.1 and 36.8. The torque acting on the column at the steady status $T_y = -0.17$ is obtained, indicating the column rotates toward $\theta = 0°$. The magnitude of T_y (i.e., 0.17), in comparison to that in Fig. 5, is quite small, which is reasonable because the two wake vortexes around the y axis are small and have weak asymmetry (see the streamlines around the column at time 36.8 in Fig. B2). Since the magnitude of T_y is small, the sign of T_y may be inverted by other physical processes, such as turbulence and gravity waves.

To find the equilibriums of the column, four additional simulations are carried out that use the same setup as the first one except for $\theta = 0°$, 15°, 20°, and 30°. Their modeled torque T_y is displayed against θ in Fig. B3 via the dashed line, showing the hexagonal column has a stable equilibrium at $\theta = 0°$. On the other hand, the modeled $T_y \neq 0$ at $\theta = 30°$ differs from the expectation of $T_y = 0$ for column symmetry, which is attributed to the orientation of cubic grid cells that breaks the column symmetry with respect to $\theta = 30°$ (Hashino et al. 2016). To represent the column symmetry at $\theta = 30°$ properly, the coordinate system, (x', y', z'), is rotated around the y axis for 30° so that the x' axis is parallel to one side face of the hexagonal column. A new simulation is then carried out for $\theta = 30°$, achieving $T_y = 0$. With the new model setup, four other simulations are carried out too with $\theta = 15°$, 20°, 40°, and 45°, and their modeled T_y is displayed in Fig. B3.

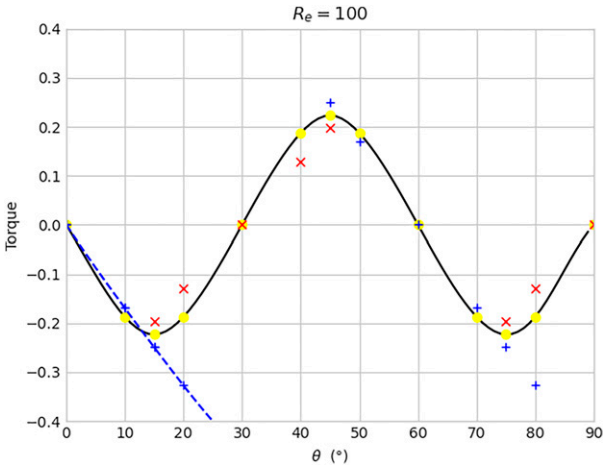

FIG. B3. Torque T_y vs θ for a symmetric hexagonal column with $L/D = 4$ and Re = 100. The blue + symbol represents the model result with the coordinate system in Fig. B1; the red × symbol is the model result with the coordinate system whose x' axis aligns along a side face of the column. The yellow symbol and black line represent the average results by synthesizing all the model results based on the column symmetry.

By synthesizing all the simulations with the two model setups based on column symmetry, a solid line in Fig. B3 is obtained to represent T_y versus θ. The solid line shows that the hexagonal column has stable equilibrium at $\theta = 0°$ and 60° and unstable equilibrium at $\theta = 30°$ and 90°. This result is consistent with the laboratory observations of Westbrook (2011) that for regular prisms two prism facets align vertically instead of horizontally.

REFERENCES

Arakawa, A., and V. R. Lamb, 1981: A potential enstrophy and energy conserving scheme for the shallow water equations. *Mon. Wea. Rev.*, **109**, 18–36, https://doi.org/10.1175/1520-0493(1981)109<0018:APEAEC>2.0.CO;2.

Auer, A. H., Jr., and D. L. Veal, 1970: The dimension of ice crystals in natural clouds. *J. Atmos. Sci.*, **27**, 919–926, https://doi.org/10.1175/1520-0469(1970)027<0919:TDOICI>2.0.CO;2.

Bailey, M., and J. Hallett, 2004: Growth rates and habits of ice crystals between −20° and −70°C. *J. Atmos. Sci.*, **61**, 514–544, https://doi.org/10.1175/1520-0469(2004)061<0514:GRAHOI>2.0.CO;2.

Bréon, F.-M., and B. Dubrulle, 2004: Horizontally oriented plates in clouds. *J. Atmos. Sci.*, **61**, 2888–2898, https://doi.org/10.1175/JAS-3309.1.

Cheng, K.-Y., P. K. Wang, and T. Hashino, 2015: A numerical study on the attitudes and aerodynamics of freely falling hexagonal ice plates. *J. Atmos. Sci.*, **72**, 3685–3698, https://doi.org/10.1175/JAS-D-15-0059.1.

Clift, R., J. R. Grace, and M. E. Weber, 1978: *Bubbles, Drops and Particles.* Academic Press, 394 pp.

Cox, R. G., 1965: The steady motion of a particle of arbitrary shape at small Reynolds numbers. *J. Fluid Mech.*, **23**, 625–643, https://doi.org/10.1017/S0022112065001593.

Garrett, T. J., S. E. Yuter, C. Fallgatter, K. Shkurko, S. R. Rhodes, and J. L. Endries, 2015: Orientations and aspect ratios of falling snow. *Geophys. Res. Lett.*, **42**, 4617–4622, https://doi.org/10.1002/2015GL064040.

Goerke, M., Z. Ulanowski, G. Ritter, E. Hesse, R. R. Neely, L. Taylor, R. A. Stillwell, and P. H. Kaye, 2017: Characterizing ice particles using two-dimensional reflections of a lidar beam. *Appl. Opt.*, **56**, G188–G196, https://doi.org/10.1364/AO.56.00G188.

Gong, J., X. Zeng, D. L. Wu, and X. Li, 2018: Diurnal variation of tropical ice cloud microphysics: Evidence from Global Precipitation Measurement Microwave Imager (GPM-GMI) polar metric measurements. *Geophys. Res. Lett.*, **45**, 1185–1193, https://doi.org/10.1002/2017GL075519.

Hashino, T., M. Chiruta, D. Polzin, A. Kubicek, and P. K. Wang, 2014: Numerical simulation of the flow fields around falling ice crystals with inclined orientation and the hydrodynamic torque. *Atmos. Res.*, **150**, 79–96, https://doi.org/10.1016/j.atmosres.2014.07.003.

——, K.-Y. Cheng, C.-C. Chueh, and P. K. Wang, 2016: Numerical study of motion and stability of falling columnar crystals. *J. Atmos. Sci.*, **73**, 1923–1942, https://doi.org/10.1175/JAS-D-15-0219.1.

Heymsfield, A. J., and J. Iaquinta, 2000: Cirrus crystal terminal velocities. *J. Atmos. Sci.*, **57**, 916–938, https://doi.org/10.1175/1520-0469(2000)057<0916:CCTV>2.0.CO;2.

——, and L. M. Miloshevich, 2003: Parameterizations for the cross-sectional area and extinction of cirrus and stratiform ice cloud particles. *J. Atmos. Sci.*, **60**, 936–956, https://doi.org/10.1175/1520-0469(2003)060<0936:PFTCSA>2.0.CO;2.

——, S. Lewis, A. Bansemer, J. Iaquinta, L. M. Miloshevich, M. Kajikawa, C. Twohy, and M. R. Poellot, 2002: A general approach for deriving the properties of cirrus and stratiform ice cloud particles. *J. Atmos. Sci.*, **59**, 3–29, https://doi.org/10.1175/1520-0469(2002)059<0003:AGAFDT>2.0.CO;2.

Jayaweera, K. O. L. F., and B. J. Mason, 1965: The behavior of freely falling cylinders and cones in a viscous fluid. *J. Fluid Mech.*, **22**, 709–720, https://doi.org/10.1017/S002211206500109X.

Ji, W., and P. K. Wang, 1999: On the ventilation coefficients of falling ice crystals at low–intermediate Reynolds numbers. *J. Atmos. Sci.*, **56**, 829–836, https://doi.org/10.1175/1520-0469(1999)056<0829:VCFFIC>2.0.CO;2.

Johnson, T. A., and V. C. Patel, 1999: Flow past a sphere up to a Reynolds number of 300. *J. Fluid Mech.*, **378**, 19–70, https://doi.org/10.1017/S0022112098003206.

Kajikawa, M., 1976: Observation of falling motion of columnar snow crystals. *J. Meteor. Soc. Japan*, **54**, 276–284, https://doi.org/10.2151/jmsj1965.54.5_276.

——, 1992: Observations of the falling motion of plate-like snow crystals. Part I: The free-fall patterns and velocity. *J. Meteor. Soc. Japan*, **70**, 1–9, https://doi.org/10.2151/jmsj1965.70.1_1.

Kikuchi, M., H. Okamoto, and K. Sato, 2021: A climatological view of horizontal ice plates in clouds: Findings from nadir and off-nadir CALIPSO observations. *J. Geophys. Res. Atmos.*, **126**, e2020JD033562, https://doi.org/10.1029/2020JD033562.

Klett, J. D., 1995: Orientation model for particles in turbulence. *J. Atmos. Sci.*, **52**, 2276–2285, https://doi.org/10.1175/1520-0469(1995)052<2276:OMFPIT>2.0.CO;2.

Le Clair, B. P., A. E. Hamielec, and H. R. Pruppacher, 1970: A numerical study of the drag of a sphere at low and intermediate Reynolds numbers. *J. Atmos. Sci.*, **27**, 308–315, https://doi.org/10.1175/1520-0469(1970)027<0308:ANSOTD>2.0.CO;2.

Magono, C., and C. Lee, 1966: Meteorological classification of natural snow crystals. *J. Fac. Sci. Hokkaido Univ. Ser. 7*, **2**, 321–335.

Neely, R., III, M. Hayman, R. Stillwell, J. P. Thayer, R. M. Hardesty, M. O'Neill, M. D. Shupe, and C. Alvarez, 2013: Polarization lidar at Summit, Greenland, for the detection of cloud phase and particle orientation. *J. Atmos. Oceanic Technol.*, **30**, 1635–1655, https://doi.org/10.1175/JTECH-D-12-00101.1.

Nettesheim, J. J., and P. K. Wang, 2018: A numerical study on the aerodynamics of freely falling planar ice crystals. *J. Atmos. Sci.*, **75**, 2849–2865, https://doi.org/10.1175/JAS-D-18-0041.1.

Noel, V., and K. Sassen, 2005: Study of planar ice crystal orientations in ice clouds from scanning polarization lidar observations. *J. Appl. Meteor.*, **44**, 653–664, https://doi.org/10.1175/JAM2223.1.

——, and H. Chepfer, 2010: A global view of horizontally oriented crystals in ice clouds from Cloud-Aerosol Lidar and Infrared Pathfinder Satellite Observation (CALIPSO). *J. Geophys. Res.*, **115**, D00H23, https://doi.org/10.1029/2009JD012365.

Pruppacher, H., and J. Klett, 1997: *Microphysics of Clouds and Precipitation*. 2nd ed. Kluwer Academic, 954 pp.

Ryzhkov, A., M. Pinsky, A. Pokrovsky, and A. Khain, 2011: Polarimetric radar observation operator for a cloud model with spectral microphysics. *J. Appl. Meteor. Climatol.*, **50**, 873–894, https://doi.org/10.1175/2010JAMC2363.1.

Siewert, C., R. P. J. Kunnen, M. Meinke, and W. Schröder, 2014: Orientation statistics and settling velocity of ellipsoids in decaying turbulence. *Atmos. Res.*, **142**, 45–56, https://doi.org/10.1016/j.atmosres.2013.08.011.

Stoelinga, M. T., J. D. Locatelli, and C. P. Woods, 2007: The occurrence of "irregular" ice particles in stratiform clouds. *J. Atmos. Sci.*, **64**, 2740–2750, https://doi.org/10.1175/JAS3962.1.

Tagliavini, G., M. McCorquodale, C. Westbrook, P. Corso, Q. Krol, and M. Holzner, 2021a: Drag coefficient prediction of complex-shaped snow particles falling in air beyond the Stokes regime. *Int. J. Multiphase Flow*, **140**, 103652, https://doi.org/10.1016/j.ijmultiphaseflow.2021.103652.

——, ——, ——, and M. Holzner, 2021b: Numerical analysis of the wake of complex-shaped snow particles at moderate Reynolds number. *Phys. Fluids*, **33**, 105103, https://doi.org/10.1063/5.0064902.

Takano, Y., and K.-N. Liou, 1989: Solar radiative transfer in cirrus clouds. Part I: Single-scattering and optical properties of hexagonal ice crystals. *J. Atmos. Sci.*, **46**, 3–19, https://doi.org/10.1175/1520-0469(1989)046<0003:SRTICC>2.0.CO;2.

Westbrook, C. D., 2011: Origin of the Parry arc. *Quart. J. Roy. Meteor. Soc.*, **137**, 538–543, https://doi.org/10.1002/qj.761.

Zeng, X., 2001: Ensemble simulation of tropical convection. Ph.D. dissertation, New Mexico Institute of Mining and Technology, 124 pp.

——, 2023: Atmospheric instability and its associated oscillations in the tropics. *Atmosphere*, **14**, 433, https://doi.org/10.3390/atmos14030433.

——, G. Skofronick-Jackson, L. Tian, A. E. Emory, W. S. Olson, and R. A. Kroodsma, 2019: Analysis of the global microwave polarization data of clouds. *J. Climate*, **32**, 3–13, https://doi.org/10.1175/JCLI-D-18-0293.1.

——, Y. Wang, and B. T. MacCall, 2020: A $k - \varepsilon$ turbulence model for the stable atmosphere. *J. Atmos. Sci.*, **77**, 167–184, https://doi.org/10.1175/JAS-D-19-0085.1.

——, J. Gong, X. Li, and D. L. Wu, 2021: Modeling the radiative effect on microphysics in cirrus clouds against satellite observations. *J. Geophys. Res. Atmos.*, **126**, e2020JD033923, https://doi.org/10.1029/2020JD033923.

——, A. J. Heymsfield, Z. Ulanowski, R. R. Neely III, X. Li, J. Gong, and D. L. Wu, 2022: The radiative effect on cloud microphysics from the Arctic to the tropics. *Bull. Amer. Meteor. Soc.*, **103**, E2108–E2129, https://doi.org/10.1175/BAMS-D-21-0039.1.

Zhou, C., P. Yang, A. E. Dessler, Y. Hu, and B. A. Baum, 2012: Study of horizontally oriented ice crystals with *CALIPSO* observations and comparison with Monte Carlo radiative transfer simulations. *J. Appl. Meteor. Climatol.*, **51**, 1426–1439, https://doi.org/10.1175/JAMC-D-11-0265.1.

Zikmunda, J., and G. Vali, 1972: Fall patterns and fall velocities of rimed ice crystals. *J. Atmos. Sci.*, **29**, 1334–1347, https://doi.org/10.1175/1520-0469(1972)029<1334:FPAFVO>2.0.CO;2.